T. Ayyappan
Research Scholar

S. Vengadesan[1]
Assistant Professor
e-mail: vengades@iitm.ac.in

Department of Applied Mechanics,
IIT Madras,
Chennai 600036, India

Influence of Staggering Angle of a Rotating Rod on Flow Past a Circular Cylinder

The influence of the staggering position of a rotating rod on flow past a main circular cylinder is investigated numerically. The rod is rotated at a constant speed ratio of 3. The effect of the diameter ratio of the rotating rod is studied by considering two different diameter ratios. The investigation is carried out at a fixed pitch length of 1. The study is carried out for two Reynolds number, viz., 100 and 500. The momentum injection from the rod is found to alter the flow characteristics behind the main cylinder. For a certain arrangement of stagger angle and diameter ratio, the vortex shedding behind the main cylinder gets suppressed. The corresponding configuration for which minimum drag coefficient is achieved is suggested from this study. [DOI: 10.1115/1.2842224]

Keywords: rotating rod, staggered arrangement, drag reduction, circular cylinder

1 Introduction

Flow past a circular cylinder is of interest to fluid mechanics researchers as it has the application in many fields, and it features many behaviors observed in complex flows. Details of earlier studies are available in Blevins [1] and Zdravkovich [2]. It is well known that due to vortex shedding, the circular cylinder experiences flow induced vibration. To control the vortex shedding phenomena and to reduce the drag force on the cylinder, various techniques have been tried. The control techniques are broadly classified into active and passive. In active control, an external energy is supplied to the flow by means of mechanical devices such as jet blowing, acoustic excitation, rotating cylinder, and so on. In a passive control technique, the vortex shedding is suppressed by means of passive devices, which do not require any external driving forces. Different types of passive devices, such as circular cylinder, splitter plates, etc., were used for this purpose.

Barnes et al. [3] used a circular rod to control the flow past a cylinder. They investigated base pressure and Strouhal number for the angle of stagger (α) between 0 deg and 45 deg. In a tandem arrangement for pitch length $1.32D$ to $1.94D$ (D is the diameter of the main cylinder), shear layers from the upstream rod reattaches onto the downstream cylinder at ± 45 deg, and no vortex shedding from the upstream rod was observed. For larger gap distances, vortex shedding from both cylinders occurred.

Luo and Gan [4] experimentally studied the effect of the upstream circular rod of $d/D=0.33$ for Re in the range of $3.15 \times 10^4 - 8.8 \times 10^4$ in tandem arrangement. Lee et al. [5] experimentally investigated the effect d/D in the range of 0.133–0.267 for Re$=2 \times 10^4$ in tandem arrangement. They proposed a relation for a critical pitch length (L_{cr}/D), which is defined as the pitch length beyond which the vortex shedding from the rod starts to happen. They found that flow quantities change abruptly at this pitch length. From a flow visualization study, they found a cavity mode for a lower pitch length and a wake impingement mode for a larger pitch length.

Zhao et al. [6] numerically studied the flow around two cylinders of different diameters at Re$=500$. They investigated the effect of L/D and stagger angle with the stationary rod of d/D $=0.25$. Recently, Zhao et al. [7] simulated the turbulent flow past a main cylinder with the rod of the diameter ratio ranging from 0.1 to 0.5 by using a $k-\omega$ turbulence closure. Wang et al. [8] used an upstream rod of $d/D=0.5$ to reduce the drag on the main cylinder for Re$=8.2 \times 10^3$. They obtained maximum drag reduction due to the shielding effect of a separated shear layer of the upstream rod on the downstream cylinder at lower L/D. They found that the upstream rod can reduce the drag until the stagger angle reaches 10 deg. In all the above discussed literatures, the rod is stationary. It is well known that the rotation of an isolated circular cylinder results in the acceleration and deceleration of fluid particles on opposite sides of the cylinder based on the direction of rotation. These phenomena result in the reduction of drag, increase in lift, and vortex suppression. A brief review of the work on an isolated rotating circular cylinder is discussed below.

The basic phenomenon of the rotating circular cylinder is explained by means of the *Magnus* effect. The potential flow theory proposed by Prandtl gives the closed streamlines only when ω > 2.0 (ω is the speed ratio), at which the stagnation point is detached from the cylinder. Ingham and Tang [9] numerically investigated the steady two-dimensional flow past a rotating circular cylinder for Re$=5$ and 20, and found that the mean drag force decreases and the mean lift force increases with an increase in speed ratio. They observed that the closed streamline pattern exists for all nonzero speed ratios. Takada and Tsutahara [10] simulated flow around an impulsively rotating two-dimensional circular cylinder using the Lattice–Boltzmann method for the Reynolds number of 200 and 500 for speed ratios of 0.5 and 1.

Kang et al. [11] simulated a two-dimensional flow past an isolated circular cylinder for three different low Reynolds numbers, Re$=60$, 100, and 160, and investigated the effect of speed ratio on aerodynamic characteristics. They found that vortex shedding exists for low rotational speed, but completely suppressed beyond a certain speed ratio.

From previous studies reported so far, it is observed that the use of passive devices changes the flow pattern behind the main cylinder and results in drag reduction for some configuration. It is also known that the isolated rotating cylinder results in the suppression of vortex shedding, decrease of mean drag coefficient, and increase in mean lift coefficient. In this sense, it will be interesting to investigate the effect of an upstream rotating rod on a stationary cylinder. In the present study, the effect of a staggering angle of a constantly rotating rod on flow past a main cylinder of diameter D is analyzed numerically. In this study, rods of two

---

diameter ratios $d/D=0.2$ and 0.5 are considered. The study is carried out for two different Reynolds numbers, viz., 100 and 500. The Reynolds number is defined based on the incoming uniform velocity and diameter of the main cylinder.

2 Numerical Details

2.1 Governing Equations. The two basic fluid flow equations, viz., continuity and momentum equations in general index notations, are given as

$$\frac{\partial(u_i)}{\partial x_i} = 0 \tag{1}$$

$$\frac{\partial(u_i)}{\partial t} + \frac{\partial(u_j u_i)}{\partial x_j} = -\frac{\partial p}{\partial x_i} + \frac{1}{\text{Re}}\frac{\partial}{\partial x_j}\left[\frac{\partial u_i}{\partial x_j} + \frac{\partial u_j}{\partial x_i}\right] \tag{2}$$

where the indices i and j each go through x, y, and z taken to denote the streamwise, cross-stream and spanwise velocities (u, velocity; x, spatial coordinate; t, time; p, pressure).

2.2 Computational Domain and Grid. In this section, the computational domain and numerical details used for simulating flow past an isolated circular cylinder is discussed. The commercially available computational fluid dynamics preprocessor GAMBIT is used for generating the grid. A box-type computational domain size of $27D \times 16D$ with a structured grid in a Cartesian coordinate system is used. The streamwise direction is along the x axis, and the cross-streamwise direction is along the y axis with the origin positioned at the center of the cylinder. The upstream boundary is placed at $7D$ from the origin. This extent is slightly less than that used by Engelman and Jamina [12] and Behr et al. [13], who used an inlet boundary at $8D$, whereas Mittal et al. [14] used one at $5D$ for both isolated as well as interference cases. The outlet boundary is specified at $20D$ downstream from the origin. The same length was used by Engelman and Jamina [12] and Burbeau and Sagaut [15]. In the y direction, the boundary is kept at $8D$ from the origin. This distance is the same as the one used by Behr et al. [13] and Mittal et al. [14].

For Reynolds number $\text{Re}=500$, a three-dimensional grid with a z axis along the spanwise direction, with $z=0$ being the midspan of the cylinder, is used. Previous numerical studies for $\text{Re}=200$ and 500 (Takada and Tsutahara [10]) and for $\text{Re}=1000$ (Jester and Kallinderis [16]) were carried out with a two-dimensionality assumption. However, the instability experiment reported by Prasad and Williamson [17] and the three-dimensional floquet stability analysis performed by Barkley and Henderson [18] at subcritical Reynolds numbers showed that the dominant spanwise scales having a wavelength of approximately three to four times the cylinder diameters exist in the range $180 < \text{Re} < 240$. After this Reynolds number, the wavelength shortens to nearly one diameter. Hence, present three-dimensional simulations are carried out with the spanwise length of $3D$ along the z direction.

2.3 Numerical Approach. The governing equations are solved using a commercial solver FLUENT 6.2. The equations are discretized using a finite volume method on a collocated grid in a fully implicit form. The convective terms in momentum equations are solved using the QUICK scheme, and the SIMPLE algorithm is used for coupling the pressure and velocity terms. The second order implicit scheme is used for the time integration of each equation. At the inlet, a uniform velocity is specified. A convective boundary condition is applied at outlet the boundary. In lateral boundaries, a symmetry boundary condition is prescribed. On the cylinder wall, a no-slip boundary condition is applied. For a three-dimensional grid, a periodic boundary condition is enforced in the spanwise direction.

Table 1 Mesh independent study and comparison of bulk parameters for Re=100

| Re=100	Mesh size $(N_x \times N_y \times N_\theta)$	St	$C_{d\text{ mean}}$	$C_{l\text{ rms}}$
Grid A	$76 \times 51 \times 60$	0.156	1.34	0.145
Grid B	$110 \times 71 \times 100$	0.160	1.38	0.241
Grid C	$135 \times 105 \times 140$	0.163	1.39	0.253
Kang et al. [11]		0.164	1.34	0.236
Engelman and Jamina [12]		0.170	1.40	0.257
Mittal et al. [14]		0.164	1.32	0.230
Meneghini et al. [19]		0.165	1.37	0.257

2.4 Validation Details

2.4.1 Grid Independence Test for a Single Stationary Cylinder. Mesh sensitivity studies are carried out for Reynolds number $\text{Re}=100$ for the case of flow past a stationary isolated cylinder with three different grids. The comparison details are given in Table 1. In that table, $Nx \times Ny \times N\theta$ denotes the number of grid points used along the streamwise, cross-stream, and circumference of the cylinder. In Grid A, the first grid point is placed at a distance of $0.05D$ from the cylinder wall. In Grids B and C, the first grid point is placed at $0.01D$ and $0.007D$, respectively. The solution is initiated and allowed to march in time with an increment of $dt=2\times10^{-2}$ until the vortex shedding becomes periodic. The simulation is continued for some more vortex shedding cycles to attain the stationary flow condition, after which the time averaging is done over 20 vortex shedding cycles to obtain both bulk and field quantities. Bulk parameters such as mean drag coefficient ($C_{d\text{ mean}}$), root mean square value of lift coefficient ($C_{l\text{ rms}}$), and Strouhal number (St) reported in Table 1, showed a good agreement with numerical data. The $C_{d\text{ mean}}$ value in literature shows a scatter from 1.32 to 1.40, and present simulation results fall within this range. From the table, we also observe that the bulk parameters for Grids B and C agree well with the quoted references. Considering the computational time, the improvement showed by Grid C is negligible. Hence, further calculations are performed with Grid B. Figure 1 shows the typical grid used for isolated stationary cylinder case.

2.4.2 Rotating Isolated Circular Cylinder at Re=100. As reported in Sec. 1, many numerical and experimental studies are available for a single cylinder rotating with constant angular speed for Reynolds numbers such as $\text{Re}=5$, 20, 60, 100, and 200. The flow past a circular cylinder started impulsively from rest to rotation reaches a steady or an unsteady state depending on the Reynolds number and speed ratio. The flow past a circular cylinder rotating with constant angular speed is simulated to validate the numerical schemes adopted in the study.

The solver, discretization schemes, domain, construction of grid, and boundary conditions on all directions are the same as those used for the case of a stationary isolated circular cylinder. For the rotating case, on a cylinder surface, constant angular speed is applied with respect to its own axis. The angular speed is non-dimensionalized by using freestream velocity and is given as a speed ratio $\omega=\phi D/2U_\infty$. This speed ratio indicates the tangential speed of the cylinder periphery with respect to the freestream velocity.

The medium grid used for the stationary isolated cylinder is used for this simulation as well, and results are compared with Kang et al. [11]. The variation of mean aerodynamic coefficients and wall pressure coefficient with respect to speed ratio is shown in Fig. 3. For the stationary cylinder, the value of $C_{l\text{ mean}}$ is zero because of the symmetric nature of vortex shedding for each cycle. With increasing speed ratio, the magnitude of $C_{l\text{ mean}}$ increases linearly toward the negative direction. This same trend is reported by Kang et al. [11]. The mean drag coefficient obtained
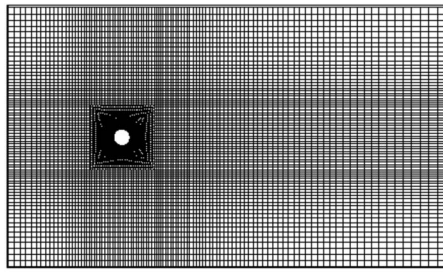
a) Complete domain
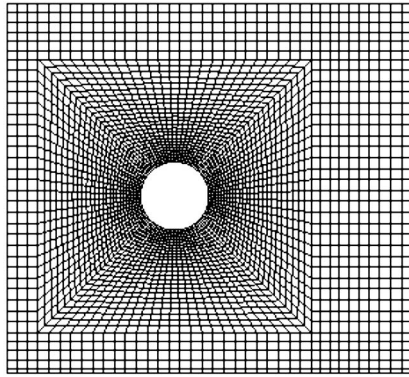

b) Enlarged view of the grid near the cylinder

Fig. 1   Typical grid used for flow over an isolated circular cylinder. (*a***) Complete domain. (***b***) Enlarged view of the grid near the cylinder.**

by the present simulation (Fig. 3(*b*)) shows the decreasing trend with increasing speed ratio. When compared with Kang et al. [11], the magnitude deviates constantly for all the speed ratios, but the same trend was obtained. The wall pressure coefficient is also found to be in good agreement with the reported references.

2.4.3   Two Circular Cylinder in Tandem Arrangement at Re=100. As the influence of the upstream rotating rod on flow past bluff bodies is our interest, it is necessary that we have to validate our solver, domain, computational scheme, and grid construction for the interference case as well. For this, the simulation of flow past two identical stationary circular cylinders in a tandem arrangement for various pitch lengths is carried out. The construction of mesh is done in the same way as it was done for the isolated case, except for the region in between two cylinders. The value of L/D at which the $C_{d \, \mathrm{mean}}$ of downstream cylinder changes abruptly is called critical pitch length (L_{cr}/D). The data from the present simulation along with those from various literatures are reported in Table 2. It is found to agree well with the experimental result of Huhe et al. [20]. The numerical results of Sharman et al. [21] and Li et al. [22] predicted lower values of L_{cr}/D.

Table 2   Comparison of critical pitch length (L_{cr}/D) for two identical cylinders in tandem arrangement at Re=100

References	L_{cr}/D	
Present	$4.25 \leqslant L_{\mathrm{cr}}/D \leqslant 4.75$	Numerical
Huhe et al. [20]	$4.5 \leqslant L_{\mathrm{cr}}/D \leqslant 5$	Experimental
Sharman et al. [21]	$3.75 \leqslant L_{\mathrm{cr}}/D \leqslant 4$	Numerical
Li et al. [22]	$3 \leqslant L_{\mathrm{cr}}/D \leqslant 4$	Numerical
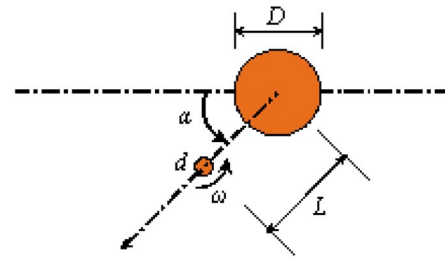
Fig. 2   Schematic arrangement of the present study

2.5   Schematic Arrangement and Other Details for the Present Study. The schematic arrangement of the present study is shown in Fig. 2. The circular cylinder having diameter D is used as the stationary main cylinder. A rod is a small circular cylinder of diameter d and is positioned on the upstream side of the main cylinder. The center-to-center distance between the rod and the main cylinder is denoted as L, which is nondimensionalized with the diameter of the main cylinder (D). The extension of computational domain from the center of the rod and the main cylinder is same as the one used for the isolated cylinder. The strategies adopted for the construction of grids in upstream, downstream, and two sidewise regions are the same as those adopted in the case of the isolated cylinder. Along the circumference of rod (θ), 60 and 80 number of grid points are taken, respectively, for d/D =0.2 and 0.5. For the rod, the first point is kept at a distance of 0.005D from the wall.

The angle of stagger (α) is varied nonuniformly from the tandem arrangement to the side-by-side arrangement. From Barnes et al. [3] and Wang et al. [8], it is observed that for a stationary rod at a lower staggering angle, the influence of rod is greater compared to that of the higher staggering angle. Hence, in this study, near by tandem line stagger angle is changed by a small value. The staggering angles used for the present simulation are 0 deg, 3 deg, 5 deg, 10 deg, 45 deg, and 90 deg. In the present study, the speed ratio is kept constant at $\omega=3$, where $\omega=\phi D/2U_\infty$ and (ϕ) is the angular velocity.

3   Results and Discussion

There are many ways to present the results obtained by current simulations. Luo and Gan, [4], Tsutsui and Igarashi, [23] and Lee et al. [5] presented their results with respect to the effect of L/D as their investigations were limited to the tandem arrangement. On the other hand, Barnes et al. [3] and Wang et al. [8] explained theirs by means of the influence of stagger angle as they did not study the influence of the speed ratio. In this paper, the results are presented as the effect of stagger angle for a constant speed of rotation $\omega=3$. The characteristics of aerodynamic coefficients, profiles of velocity at different wake stations, and streamline patterns are discussed in the following section.

3.1   Simulation Results at Re=100. The flow Reynolds number based on the main cylinder diameter for this case is 100. In this section, the effect of the diameter ratio of rod is analyzed by using the rod of diameter ratios 0.2 and 0.5.

3.1.1   Aerodynamic Coefficients

3.1.1.1   Variation of $C_{d \, \mathrm{mean}}$. The variation of the mean drag coefficient of the main cylinder is shown in Fig. 4(*a*). For the rod of d/D=0.2, the mean value of $C_{d \, \mathrm{mean}}$ increases continuously up to the stagger angle of 45 deg and then decreases for a side-by-side arrangement. The magnitude of $C_{d \, \mathrm{mean}}$ alternatively decreases and increases for the rod of d/D=0.5. The minimum value of the drag coefficient is observed at the staggering angle of 10 deg for d/D=0.5. For both diameter ratios, the drag acting on
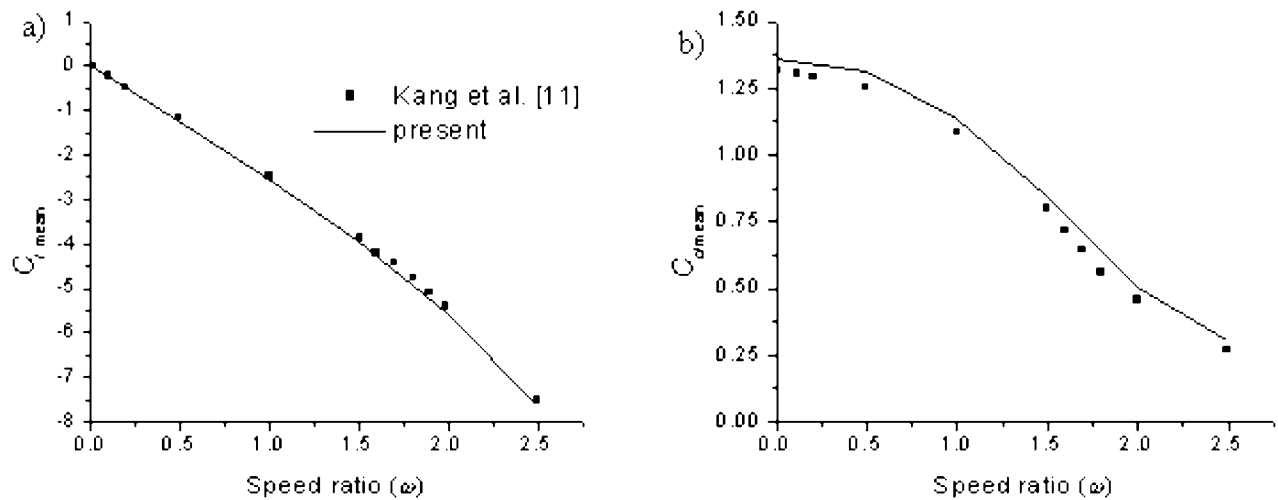
a) Variation of Mean lift coefficient, **b)** Variation of Mean drag coefficient
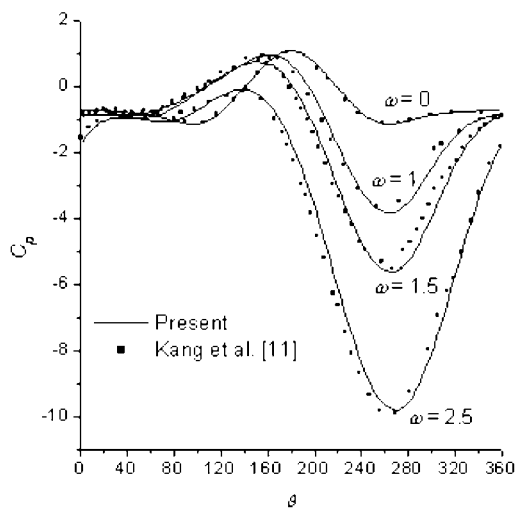
**c)** Variation of wall pressure coefficient with speed ratio.

Fig. 3 Results for the isolated rotating cylinder. Legends are the same in both plots. (*a*) Variation of mean lift coefficient. (*b*) Variation of mean drag coefficient. (*c*) Variation of wall pressure coefficient with speed ratio.

the main cylinder is less than the value of the isolated stationary cylinder (Table 1). This drastic change in the $C_{d \text{ mean}}$ can be explained with the help of the mean streamline plot shown in Fig. 5 for $\alpha=0$ deg and 10 deg. Because of the rotation of the rod, the fluid in the gap region gets decelerated and creates a recirculation bubble in front of the main cylinder. This causes negative pressure distribution in that area. For both tandem and 10 deg stagger angles, the negative region extends to the wake behind the main cylinder and forms a dumbbell shape. This dumbbell shape is not observed for the rod of $d/D=0.2$. For the sake of completeness, the mean drag coefficients of the rod for both diameter ratios are also given in Fig. 4(*d*). For both d/D, it shows a decreasing trend with increasing stagger angle up to 45 deg and then almost stays constant.

3.1.1.2 Variation of $C_{l \text{ mean}}$. Figure 4(*b*) shows the variation of the mean lift coefficient of the main cylinder with respect to the positioning of the rotating rod. For lower stagger angles, the value continuously decreases with the rod of $d/D=0.2$. Whereas for the rod of $d/D=0.5$, this magnitude slightly increases for lower stag-

ger angles' and then it decreases continuously. For all the cases considered in this study, the $C_{l \text{ mean}}$ value stays nonzero. This is due to the asymmetry nature of pressure distribution on the main cylinder because of the rotation of the rod.

3.1.1.3 Variation of $C_{l \text{ rms}}$. The variation of the root mean square value of lift coefficient ($C_{l \text{ rms}}$) shown in Fig. 4(*c*) depicts a favorable trend in vortex suppression. With the rotating rod of $d/D=0.2$, a magnitude of $C_{l \text{ rms}}$ decreases continuously with increasing stagger angle. This value attains zero for $\alpha=90$ deg, and the flow behind the main cylinder is steady. This steady flow behind the main cylinder can be observed in the instantaneous vorticity contour. Figure 6(*a*) shows the instantaneous vorticity plot for $d/D=0.2$ at the 90 deg stagger angle. This vorticity contour is at a time instant corresponding to the maximum positive lift of the main cylinder. For a better comparison, the simulation is carried out for the stationary rod of the same d/D and is given in Fig. 6(*a*). (i) Nice periodic counter rotating vortices are observed behind the main cylinder for the stationary rod, whereas at $\omega=3$
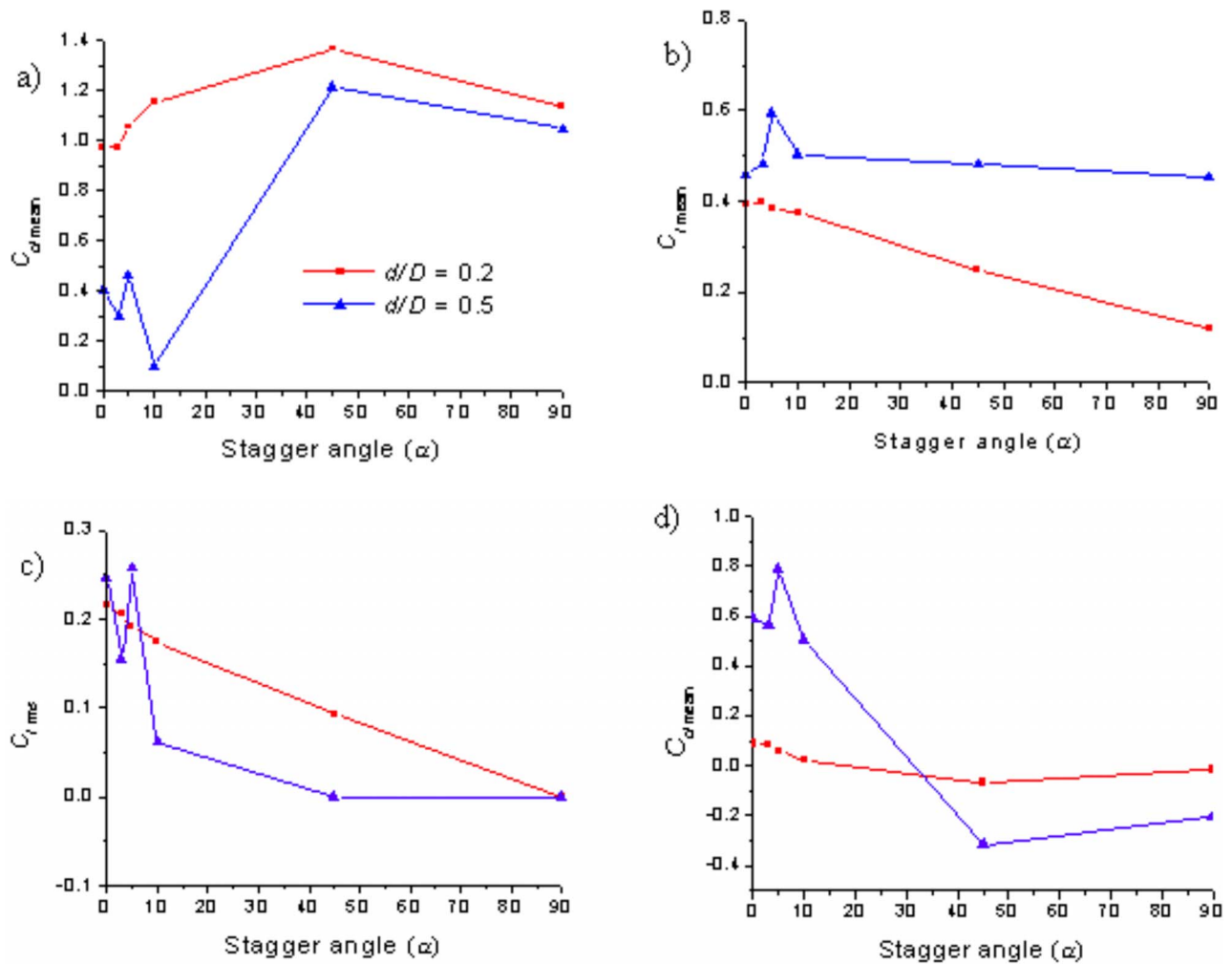
Fig. 4 Variation of aerodynamic coefficients. (*a*) Mean drag coefficient of the main cylinder. (*b*) Mean lift coefficient of the main cylinder. (*c*) rms lift coefficient of the main cylinder. (*d*) Mean drag coefficient of the rod. Legends are the same in all plots.

(Fig. 6(*a*) (ii)), the contours are stretched. The flow does not show features changing with respect to time, and the vortex shedding behind the main cylinder is suppressed. A similar behavior is observed for both 45 deg and 90 deg with the rod of diameter ratio 0.5, as shown in Figs. 6(*b*) and 6(*c*), respectively. The contours of
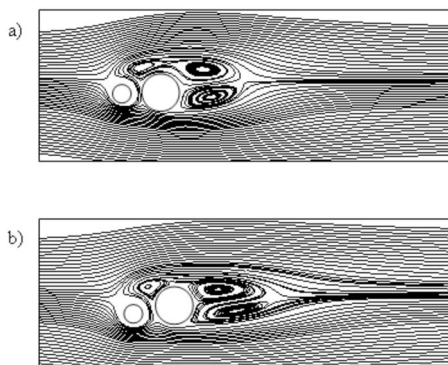

Fig. 5 Mean streamline contours for *d*/*D*=0.5. (*a*) Tandem arrangement. (*b*) Staggering angle of 10 deg.

u_{rms} shown in Fig. 7 for a typical case also confirm the trend. The value is very low when the rod is subjected to rotation.

3.1.2 Variation of Mean Velocity. The variation of mean velocity in the field shows how the supplied momentum through the rotation of the rod is convected to various regions of the flow field. Figure 8(*a*) shows the variation in mean streamwise velocity along the wake centerline of the main cylinder for the rotating rod of *d*/*D*=0.2. For the tandem arrangement, a small positive velocity region is observed in front of the main cylinder. This indicates that the direction of flow crosses the centerline. For small staggering angles, negative velocity is observed in the gap region. This is because of the continuous deceleration of flow in the positive *y* direction. The velocity profile behind the main cylinder is not affected for tandem and small stagger angles. However, for 45 deg and 90 deg, the flow is considerably affected behind the main cylinder. In the side-by-side arrangement, the recirculation region is not observed behind the main cylinder. The velocity profile becomes almost flat without any negative velocity, and the freestream recovery is delayed.

The respective velocity variation for the rotating rod of *d*/*D* =0.5 is shown in Fig. 8(*b*). For the tandem arrangement and for other lower stagger angles, a negative velocity region is observed in between gaps. Behind the main cylinder, the velocity profile changes considerably for each staggering angle. However, for the

(a)

(b)

(c)
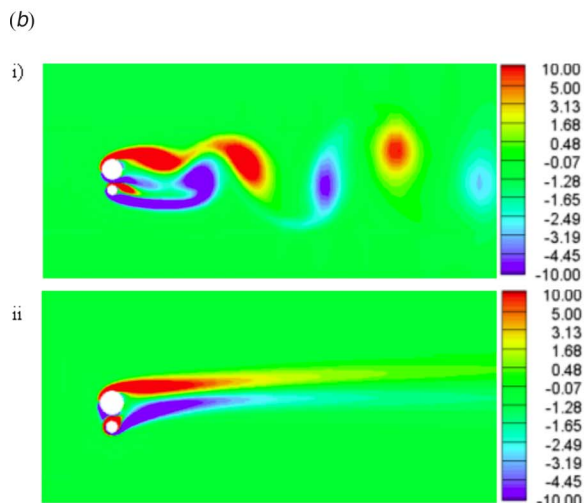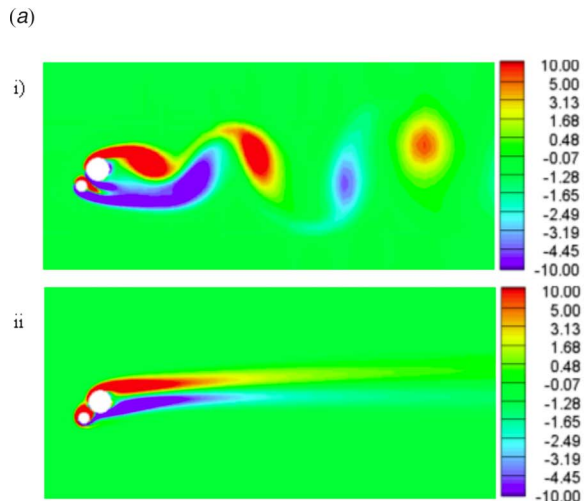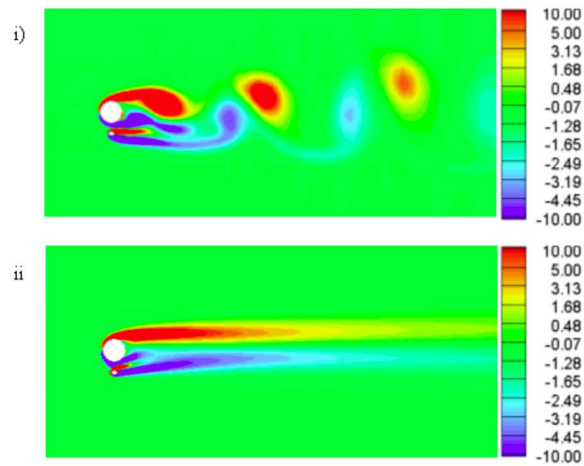
Fig. 6 (*a*) **Instantaneous vorticity contour for** *d*/*D*=0.2 **and** α =90 **deg: (i)** ω=0 **and (ii)** ω=3. (*b*) **Instantaneous vorticity contour for** *d*/*D*=0.5 **and** α=45 **deg: (i)** ω=0 **and (ii)** ω=3. (*c*) **Instantaneous vorticity contour for** *d*/*D*=0.5 **and** α=90 **deg: (i)** ω=0 **and (ii)** ω=3.

rod of diameter ratio 0.2 in tandem as well as low staggering angles, the velocity profile coincides with one another. For the rod of *d*/*D*=0.2, the velocity profile along the normal plane at *x*=0 is shown in Fig. 9(*a*). In this plot, the velocities in the positive *y* direction (i.e., above the cylinder) coincide with each other for all
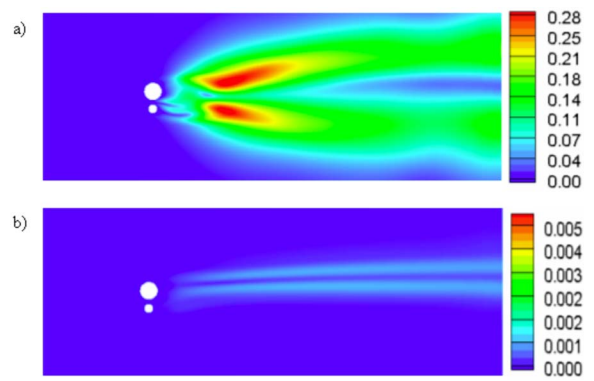

Fig. 7 u_{rms} **contour for** (*a*) *d*/*D*=0.5, α=0 **deg, and** ω=0 **and** (*b*) *d*/*D*=0.5, α=0 **deg, and** ω=3

the cases. On the other hand, for the rod of *d*/*D*=0.5, which is shown in Fig. 9(*b*), a negative velocity profile is observed for lower staggering angles. This could be again due to the formation of the recirculation region in front of the main cylinder.

(a)

(b)
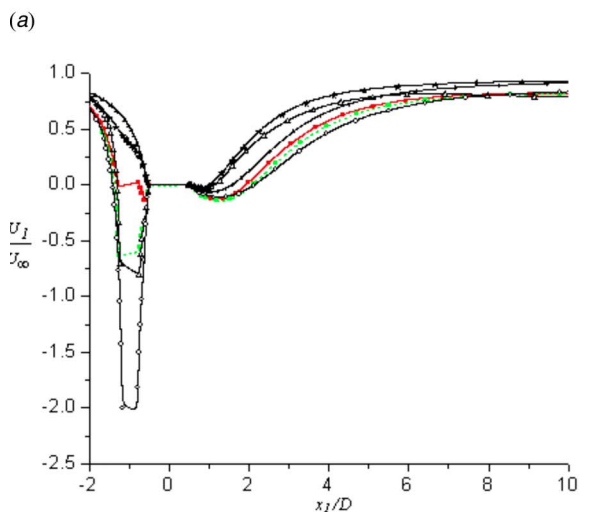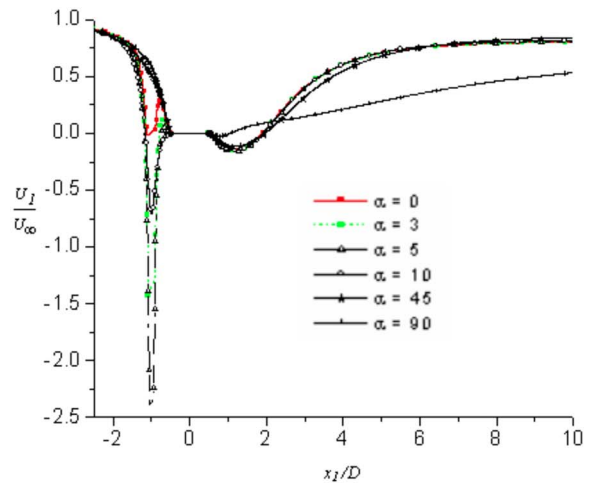
Fig. 8 **Mean streamwise velocity along the wake centerline for** (*a*) *d*/*D*=0.2 **and** (*b*) *d*/*D*=0.5. **Legends are the same in both plots.**

(a)

(b)
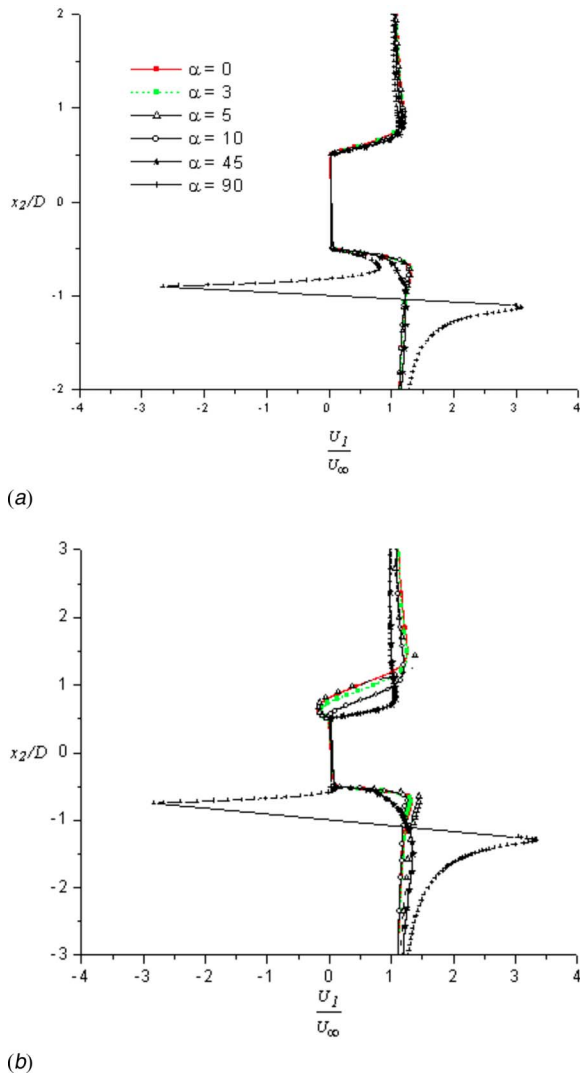
Fig. 9 (*a*) **Variation of mean streamwise velocity along a normal line at** $x_1/D=0$ **for Re=100 and** $d/D=0.2$. (*b*) **Variation of mean streamwise velocity along a normal line at** $x_1/D=0$ **for Re=100 and** $d/D=0.5$. **Legends are the same in both plots.**

3.2 Simulation Results at Re=500. To investigate the effect of Reynolds number, the present study is extended to Re=500. Though the flow becomes turbulent at this Re, from available literature there is no clear information about what is the good or right turbulence model even for flow past an isolated circular cylinder as they all show some kind of discrepancy in predictions. Large eddy simulation (LES) or direct numerical simulation (DNS) techniques are computationally expensive methods for the present study. Hence, we perform simulations for this case also with the laminar flow model as this assumption may not have any serious influence on aerodynamic quantities and mean velocities, and, hence, on the conclusions with respect to the objective of the present study.

However, for reasons mentioned in Sec. 2.2, three-dimensional simulations are carried out. A mesh independent study is carried out for this case as well. The grid size in the streamwise and cross-streamwise directions are kept the same as the one used for Re=100 case. In the spanwise direction, the domain is chosen as $3D$ (Ayyappan [24]) and the number of mesh points is varied as 20, 26, and 32, respectively, for three grids, namely, Grids D, E, and F. Drag coefficients computed by these grids for the case of flow past an isolated cylinder are compared in Table 3. From the

Table 3 Comparison of bulk parameters for Re=500

Re=500	Mesh size $(x \times y \times \theta \times z)$	$C_{d\ mean}$
Grid D	$110 \times 71 \times 100 \times 20$	1.217
Grid E	$110 \times 71 \times 100 \times 26$	1.114
Grid F	$110 \times 71 \times 100 \times 32$	1.085
Wen et al. [25]		1.143

table, we observe that there is a 10% variation between Grids D and E and a 3% variation between Grids E and F. Hence, further calculations are run with Grid F. The contours of streamwise vorticity are presented in Fig. 10 for two representative cases. They show the presence of a vortical structure in the spanwise direction, which indicates the need for carrying out three-dimensional calculations. For this Reynolds number also, a control rod with two different diameter ratios is considered. The results are also compared with those for Re=100.

3.2.1 Aerodynamic Coefficients

3.2.1.1 Variation of $C_{d\ mean}$. The variation of the mean drag coefficient of the main cylinder with respect to the angular position of the rotating rod is given in Fig. 11(*a*). With the rod of $d/D=0.2$, the drag value slightly increases for lower stagger angles and decreases for higher stagger angles. The opposite behavior of drag coefficient is found to occur with the rod of $d/D=0.5$. A minimum mean drag value is observed at a 10 deg stagger angle with the rod of diameter ratio of 0.5. It is observed that for both Re=100 and 500, the trend is the same for both diameter ratios. Once again, the mean drag of the rod for both diameter ratios is also given in Fig. 11(*d*). For both ratios, it shows a decreasing trend with increasing stagger angle up to 45 deg and then a marginal rise.

3.2.1.2 Variation of $C_{l\ mean}$. Figure 11(*b*) shows the variation of the mean lift coefficient of the main cylinder by the influence of the staggering angle. This value constantly decreases for the main cylinder when the rod of $d/D=0.2$ is placed at various staggering angles. For the rod of $d/D=0.5$, the $C_{l\ mean}$ value slightly increases at lower staggering angles. This value decreases with further increase in staggering angle and reaches a minimum value for the side-by-side arrangement, which is also observed for the Reynolds number of 100.

3.2.1.3 Variation of $C_{l\ rms}$. The variation of $C_{l\ rms}$ of the main cylinder with respect to the positioning of the rotating rod is shown in Fig. 11(*c*). For the rod of $d/D=0.2$, this value slightly increases first and then decreases. Again, this value increases in the side-by-side arrangement, whereas this value for the rod of $d/D=0.5$ slightly oscillates for lower stagger angles and then constantly decreases as the stagger angle increases. A minimum $C_{l\ rms}$ of magnitude 0.05 is observed in the side-by-side arrangement. The suppression of vortex shedding observed for the Re=100 case is not observed here.

3.2.2 Variation of Velocity. The variation of the mean streamwise velocity component along the normal plane at $x=0$ for $d/D=0.5$ is shown in Fig. 12(*a*). At $x=0$, a maximum negative velocity in the region closer to the positive y direction is observed for the tandem arrangement. As the angle of stagger increases, the negative velocity region in the positive y direction changes to a positive magnitude. A small wake is observed behind the main cylinder for the 45 deg stagger angle. For the side-by-side arrangement, a steep velocity gradient is observed near the rotating rod. The same velocity component at $x/D=1$ is shown in Fig. 12(*b*). The reduction in width of the wake is observed as the stagger angle increases. The velocity gradient behind the rod disappears, and the wakes from the cylinder and the rod merge.
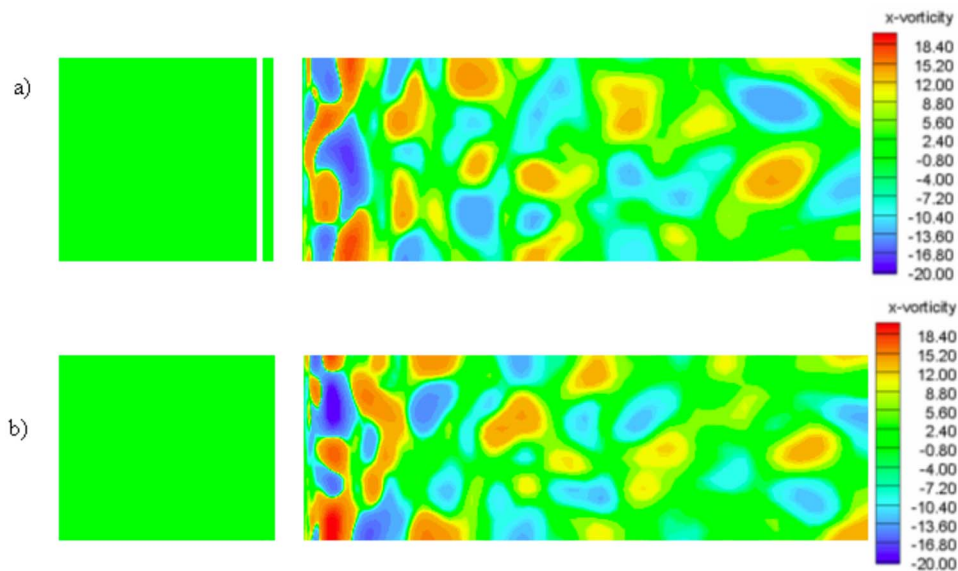
Fig. 10   Contours of streamwise vorticity for the case of $d/D=0.2$ and $\omega=3$. (*a*) $\alpha=0$ deg; (*b*) $\alpha=90$ deg.
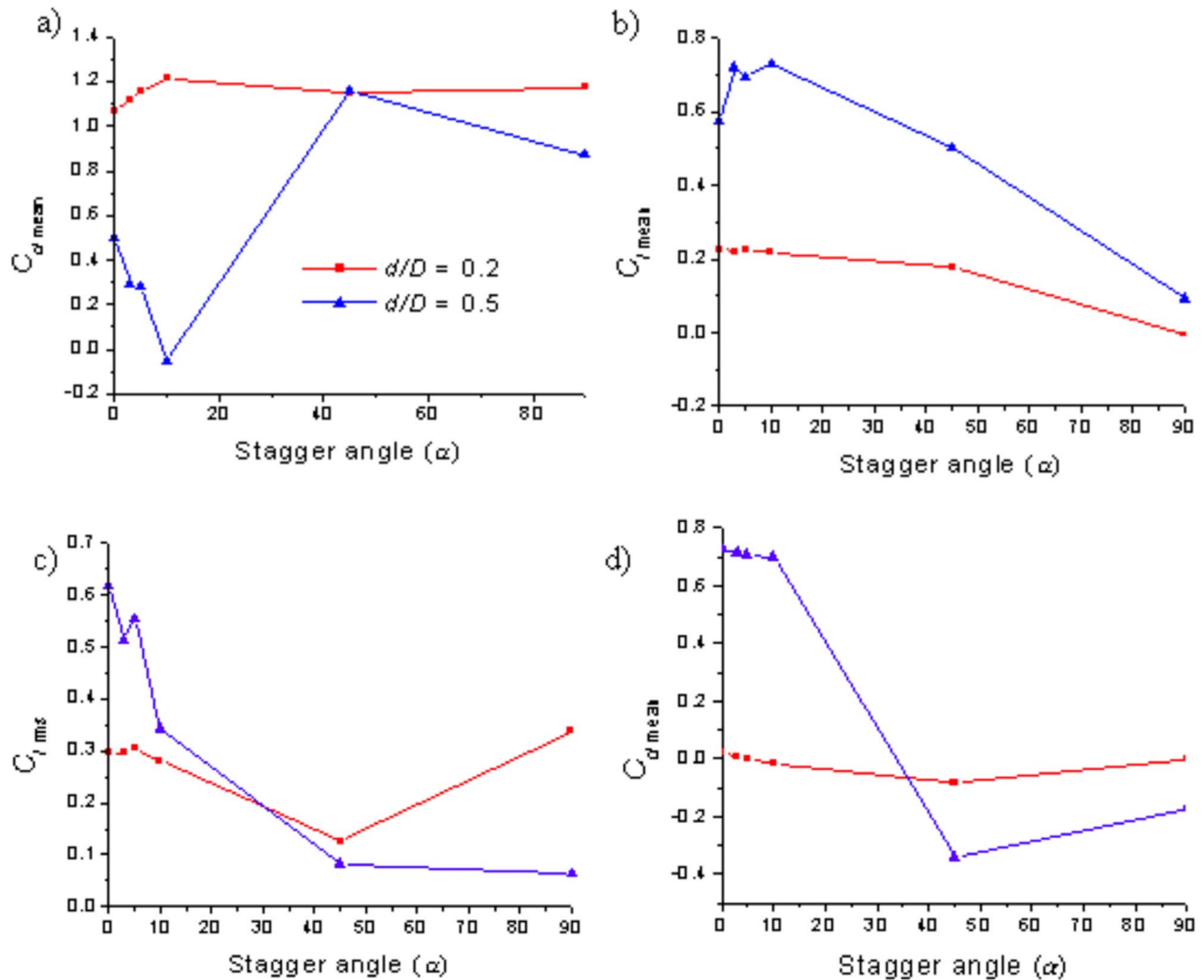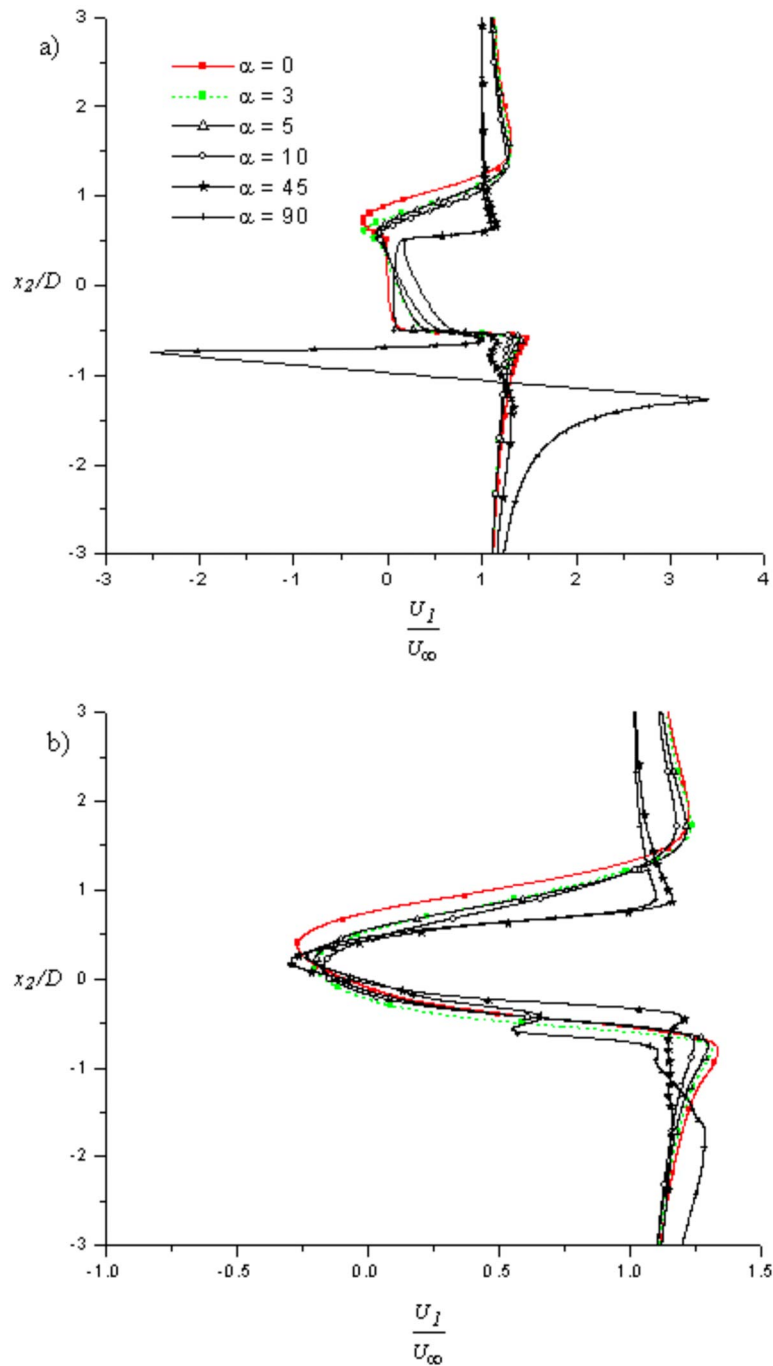

Fig. 11   Variation of aerodynamic coefficients. (*a*) Mean drag coefficient of the main cylinder. (*b*) Mean lift coefficient of the main cylinder. (*c*) rms lift coefficient of the main cylinder. (*d*) Mean drag coefficient of the rod. Legends are the same in all plots.

Fig. 12 Variation of mean streamwise velocity along a normal line for $d/D=0.5$ and Re=500. (a) $x/D=0$; (b) $x/D=1$. Legends are the same in both plots.

3.3 Maximum Drag Reduction. In previous sections, the variation of aerodynamic coefficients of the main cylinder and velocity profile in the flow field with respect to the positioning of the rotating rod is discussed. The variation of the mean drag of the control rod is also observed independently. However, the drag acting on the rod contributes a small increase when considered as a system along with the main cylinder. Hence, the mean system drag ($C_{d\,sys}$) is calculated by using the formula $C_{d\,sys}=C_{d\,main}+d/D\mathrm{x}(C_{d\,rod})$, as reported by Luo and Gan [4]. This formula is a simple arithmetic addition of mean drag for the main cylinder and the rod nondimensionalized by the main cylinder diameter (D),

and the variation for all the cases considered is shown in Fig. 13(a). The optimum configuration in comparison with drag in the corresponding stationary case is listed in Table 4. As can be observed, at Re=100 for the $d/D=0.2$ case, a minimum system drag observed is at the stagger angle of 3 deg, whereas this position is 10 deg for the $d/D=0.5$ rod. However, based on the magnitude of drag, maximum reduction is observed with the rod of $d/D=0.5$. The minimum system drag obtained for this Reynolds number is 0.598, corresponding to the case $d/D=0.5$ and $\alpha=10$ deg. The $C_{d\,sys}$ obtained for the Reynolds number Re=500 is 0.647, corresponding to the case $d/D=0.5$ and $\alpha=10$ deg. The same arrange-

Journal of Fluids Engineering

(a)

(b)
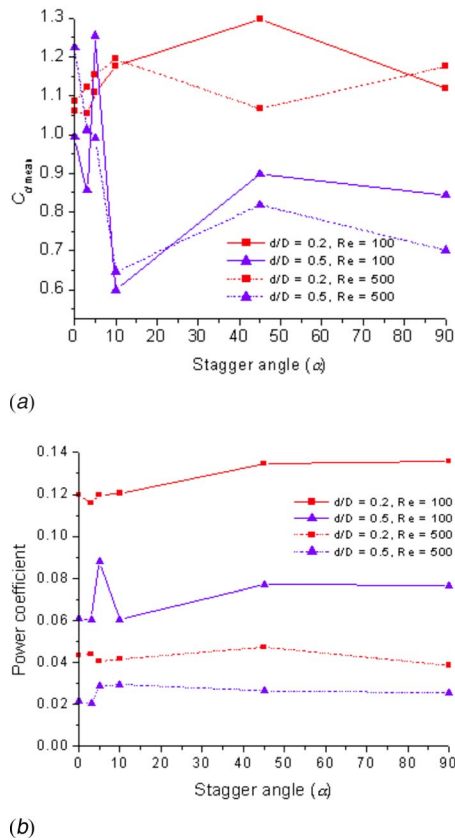
Fig. 13 Variation of system drag for both diameter ratios and Reynolds numbers

ment and speed ratio are found to give a minimum drag for both Reynolds numbers considered in the present study.

3.4 Power Coefficient. The total power required (P_{tot}) for any particular configuration is the summation of translational (P_{trans}) and rotational power (P_{rot}). P_{trans} is the drag coefficient of the system and P_{rot} is the power coefficient of the rotating rod. Power coefficient (P_{rot}) is calculated from the nondimensionalized wall shear stress acting on the rod (σ_W), speed ratio (ω), and diameter ratio (d/D) as $P_{tot} = \sigma_w \omega (d/D)$. The power coefficient required to rotate the rod is given in Fig. 13(b). The magnitude of power coefficient for a particular configuration is the same for all the stagger angles. In the near tandem arrangement, the magnitude slightly fluctuates. This is because of the presence of the main cylinder. For the rod of $d/D=0.2$ at Re=100, the power coefficient calculated lies closer to 0.12. This value reduces to 0.06 for the rod of $d/D=0.5$ for the same Reynolds number. This reduction in power required to rotate the rod with the increase in d/D is observed for Re=500 also. The total power coefficient of the minimum drag coefficient configuration is 0.718 for Re=100 and

0.697 for Re=500. This value is less when compared to the system drag (Table 4) for the corresponding case of the stationary rod.

4 Conclusions

The influence of the rotating rod on flow past a main circular cylinder is investigated numerically. The effect of the staggering position of the rod on aerodynamic coefficients is analyzed. A common phenomenon of increase in the velocity behind the rotating rod is observed, and the reason is attributed to the momentum transfer. With the rod of diameter ratio of 0.2, vortex suppression behind the main cylinder is observed for Re=100 in the side-by-side arrangement. This vortex suppression phenomenon is observed for 45 deg stagger angle and in the side-by-side arrangement with the rod of diameter ratio of 0.5. The optimum position for a maximum drag reduction is calculated by considering system drag. The staggering position is found to be at 10 deg from the stagnation point of the isolated cylinder. The same position of the staggering angle and speed ratio is obtained for both the Reynolds numbers considered in this study. It is observed that the total power required for the minimum system drag configuration is less than that for the stationary rod case.

Nomenclature

D = diameter of the main cylinder
f = frequency of vortex shedding
d = diameter of the upstream rod
L = pitch length
L_{cr} = critical pitch length
ω = speed ratio ($\phi D/2U_\infty$)
ϕ = angular velocity
α = stagger angle
U = freestream velocity
St = Strouhal number
x_i = spatial coordinate
p = pressure
ν = kinematic viscosity
Re = Reynolds number ($U_\infty D/\nu$)
C_d = coefficient of drag

Subscripts

rms = root mean square
main = main cylinder
sys = system
rod = upstream rod
trans = translational
rot = rotational

References

[1] Blevins, R. D., 1977, *Flow Induced Vibrations*, Van Nostrand Reinhold, New York.
[2] Zdravkovich, M. M., 1997, *Flow Around Circular Cylinders*, Oxford University Press, New York.
[3] Barnes, F. H., Baxendale, A. J., and Grant, I., 1985, "The Flow Past Two Cylinders Having Different Diameters," Aeronaut. J., **89**, pp. 125–134.
[4] Luo, S. C., and Gan, T. L., 1992, "Flow Past Two Tandem Circular Cylinders of Unequal Diameter," Aeronaut. J., **96**, pp. 105–114.
[5] Lee, S. J., Lee, S. I., and Park, C. W., 2004, "Reducing the Drag on a Circular Cylinder by Upstream Installation of a Small Control Rod," Fluid Dyn. Res., **34**, pp. 233–250.
[6] Zhao, M., Cheng, L., Teng, B., and Liang, D., 2005, "Numerical Simulation of Viscous Flow Past Two Circular Cylinders of Different Diameters," Appl. Ocean. Res., **27**, pp. 39—55.
[7] Zhao, M., Cheng, L., Teng, B., and Dong, G., 2007, "Hydrodynamic Forces on Dual Cylinders of Different Diameters in Steady Currents," J. Fluids Struct., **23**, pp. 59–83.
[8] Wang, J. J., Zhang, P. F., Lu, S. F., and Wu, K., 2006, "Drag Reduction of a Circular Cylinder Using an Upstream Rod," Flow, Turbul. Combust., **76**, pp. 83–101.
[9] Ingham, D. B., and Tang, T., 1990, "A Numerical Investigation Into the Steady Flow Past a Rotating Circular Cylinder at Low and Intermediate Reynolds Numbers," J. Comput. Phys., **87**, pp. 91–107.
[10] Takada, N., and Tsutahara, M., 1998, "Evaluation of Viscous Flow Around a

Table 4 Optimum configuration for drag reduction

Re	d/D	α (deg)	$C_{d\ sys}$	For stationary rod
100	0.2	3	1.053	1.105
	0.5	10	0.598	1.014
500	0.2	45	1.066	1.127
	0.5	10	0.647	0.869

Suddenly Rotating Circular Cylinder in the Lattice Boltzmann Method," Comput. Fluids, **27**, pp. 807–828.

[11] Kang, S., Choi, H., and Lee, S., 1999, "Laminar Flow Past a Rotating Circular Cylinder," Phys. Fluids, **11**(11), pp. 3312–3321.

[12] Engelman, S. M., and Jamnia, M. A., 1990, "Transient Flow Past a Circular Cylinder: A Bench Mark Solution," Int. J. Numer. Methods Fluids, **11**, pp. 985–1000.

[13] Behr, M., Liou, J., Shih, R., and Tezduyar, T. E., 1991, "Vorticity-Stream Function Formulation of Unsteady Incompressible Flow Past a Cylinder: Sensitivity of the Computed Flow Field to the Location of the Outflow Boundary," Int. J. Numer. Methods Fluids, **12**, pp. 323–342.

[14] Mittal, S., Kumar, V., and Raghuvanshi, A., 1997, "Unsteady Incompressible Flows Past Two Cylinders in Tandem and Staggered Arrangements," Int. J. Numer. Methods Fluids, **25**, pp. 1315–1344.

[15] Burbeau, A., and Sagaut, P., 2002, "Simulation of a Viscous Compressible Flow Past a Circular Cylinder With High-Order Discontinuous Galerkin Methods," Comput. Fluids, **31**, pp. 867–889.

[16] Jester, W., and Kallinderis, Y., 2003, "Numerical Study of Incompressible Flow About Fixed Cylinder Pairs," J. Fluids Struct., **17**, pp. 561–577.

[17] Prasad, A., and Williamson, C. H. K., 1997, "The Instability of the Shear Layer Separating From a Bluff Body," J. Fluid Mech., **333**, pp. 375–402.

[18] Barkley, D., and Henderson, D. R., 1996, "Three-Dimensional Floquet Stability Analysis of the Wake of a Circular Cylinder," J. Fluid Mech., **322**, pp. 215–241.

[19] Meneghini, J. R., Saltara, F., Siqueria, C. L. R., and Ferrari, J. A., 2001, "Numerical Simulation of Flow Interference Between Two Circular Cylinders in Tandem and Side-By-Side Arrangements," J. Fluids Struct., **17**, pp. 561–577.

[20] Huhe, A., Tatsuno, M., and Taneda., S., 1985, "Visual Studies on Wake Structure Behind Two Cylinders in Tandem Arrangement," Rep. Res. Inst. Appl. Mech. (Kyushu Univ.), **32**(99), pp. 1–20 (data taken from Sharman et al., Ref. 21).

[21] Sharman, B., Lien, F. S., Davidson, L., and Norberg, C., 2005, "Numerical Predictions of Low Reynolds Number Flows Over Two Tandem Circular Cylinders," Int. J. Numer. Methods Fluids, **47**(5), pp. 427–447.

[22] Li, J., Chambarel, A., Donneaud, M., and Martin, R., 1991, "Numerical Study of Laminar Flow Past One and Two Cylinders," Comput. Fluids, **19**, pp. 155–170.

[23] Tsutsui, T., and Igarashi, T., 2002, "Drag Reduction of a Circular Cylinder in an Air Stream," J. Wind. Eng. Ind. Aerodyn., **90**, pp. 527–541.

[24] Ayyappan, T., 2007, "Influence of Staggering Angle and Speed Ratio of Upstream Rotating Rod on Flow Past a Circular Cylinder," MS thesis, IIT Madras.

[25] Wen, C. Y., Yeh, C. L., Wang, M. J., and Lin, C. Y., 2004, "On the Drag of Two Dimensional Flow About a Circular Cylinder," Phys. Fluids, **16**(10), pp. 3828–3831.